The Structure of GeS_2-P_2S_5 Glasses

Brian Cherry and Josef W. Zwanziger*

Department of Chemistry, Indiana University, Bloomington, Indiana 47405

Bruce G. Aitken

SP-FR-05, Corning Inc., Corning, New York 14831

Received: December 19, 2001; In Final Form: July 22, 2002

Structural models of $(GeS_2)_{1-x}(P_2S_5)_x$ glasses were developed and used to explain bulk properties of the glasses, including density, glass transition temperature, and refractive index. The models were developed based on combined data from solid-state NMR measurements of spectra and magnetic dipole distributions, neutron diffraction, and Raman spectroscopy. The fundamental structural groups of these glasses consist of $GeS_{4/2}$ tetrahedra, and both $S{=}PS_{3/2}$ and $PS_{3/2}$ phosphorus units, the latter necessitating also the presence of sulfur−sulfur bonding. Furthermore, the phosphorus sites are present in both network sites and molecular clusters.

I. Introduction

Germanium sulfide glasses are practical host materials for rare-earth ions because of their large refractive index and low maximum phonon energy. These properties respectively result in large emission cross-sections and low nonradiative decay rates for optical transitions. Consequently, germanium sulfide glasses doped with rare-earths are of interest for a variety of photonic applications, including optical amplifiers and near-IR sources.[1,2] Although the structure, bulk properties, and their relationship in comparable oxides have been studied in great detail, the same is not true for sulfides. Our particular interest here is in how phosphorus, as an additive, interacts with the GeS_2 network. The compositions studied here are of the form $(GeS_2)_{1-x}(P_2S_5)_x$ and so can be viewed as sulfide glass co-former materials.

Because the bonding in sulfides is covalent to a good approximation (unlike oxides), it is also interesting to consider these glasses in light of mechanical models of glass stability that focus on short-range constraints.[3,4] To apply these models appropriately, however, it is necessary to determine the structure with some precision. Compared to systems such as Ge−As−Se,[5] for which there is essentially one coordination number for each atom, the chemistry of the Ge−P−S system is considerably richer, leading to a wider variety of structures.

The purpose of this paper is to present a structural model for germanium phosphorus sulfur glasses generated from the combined use of solid-state NMR, Raman spectroscopy, and neutron diffraction techniques. High-speed magic angle spinning (MAS) and two-dimensional phase adjusted spinning sideband (2D-PASS) NMR experiments give information on the local phosphorus environment present in the glass. Information about the distribution of phosphorus in the glass is obtained from measurement of the second moment of phosphorus−phosphorus magnetic dipole couplings, M_2. Raman spectroscopy offers a view of the bonding and polyhedra present in the glass, whereas neutron diffraction provides complementary information on the glass structure, which particularly emphasizes pair distributions involving germanium. The structural models generated are then related to bulk properties including T_g and refractive index.

When determining the structure of a glass, it is critical that multiple techniques be employed. For the Ge−P−S system, solid-state NMR and neutron diffraction complement each other quite well. For practical purposes, phosphorus is the only nucleus that is NMR-active in these materials.[6] Therefore, substantial information can be obtained about the phosphorus environment from solid-state NMR, whereas only indirect information can be acquired concerning the germanium and sulfur. In neutron diffraction, the situation is reversed. Because of the large neutron scattering cross-section of germanium and the large amount of sulfur in the samples, the germanium−germanium and germanium−sulfur partial structure factors will contribute most strongly to the total signal obtained from the experiment.[7] Consequently, information about the germanium and sulfur environment, which was lacking in the NMR spectra, is accentuated in the neutron diffraction data. Raman spectroscopy is sensitive to all species in the glass and provides information on the types of bonding and local polyhedra present. Therefore, when the data provided by NMR, neutron diffraction, and Raman spectroscopy are considered together, a relatively comprehensive model of the glass structure, even for a multicomponent system such as this, can be generated.

Previous structural investigations of the Ge−P−S system are quite limited, the primary one being that of Koudelka and Pisárčik,[8] based solely on Raman data. They studied a wide variety of glass compositions which spanned the glass forming region and concluded that the glasses are made up of $GeS_{4/2}$ tetrahedra and $S{=}PS_{3/2}$ units. They further inferred that, as compositions become richer in phosphorus, the $S{=}PS_{3/2}$ units partially dissociate into $PS_{3/2}$ units and S_8 molecules. They also noted the existence of molecular species S_8, P_4S_{10}, P_4S_9, and P_4S_7 in sulfur rich glasses. Vinogradova and Maisashvili determined the equilibrium phase diagram of the GeS_2−P_2S_5 system.[9] One of the present authors has also published some data on this system in the context of studies of Ge−As−P−S glasses.[10,11]

Much fundamental work has also been done on the parent binary systems, Ge−S and P−S. Crystal structures have been determined for various germanium sulfide and phosphorus sulfide compounds. Germanium disulfide has four crystal forms:

* To whom correspondence should be addressed. Phone: (812) 855-3994. Fax: (812) 855-8300. E-mail: jzwanzig@indiana.edu.

10.1021/jp014617u CCC: $22.00
Published on Web 10/04/2002

[12−15] a high-temperature phase (α-GeS_2), a low-temperature phase (β-GeS_2), a high temperature and high-pressure phase (γ-GeS_2), and an expanded framework phase (δ-GeS_2). Of relevance here are the low-pressure α and β phases. In the α, high temperature form, chains of corner-sharing $GeS_{4/2}$ polyhedra are bridged together by two edge-sharing $GeS_{4/2}$ polyhedra. The β form is made up entirely of corner-sharing $GeS_{4/2}$ polyhedra, which form six-membered rings. GeS_2 glass is thought to have a similar structure to α-GeS_2.[16−19]

The phosphorus−sulfur system contains many stoichiometric compounds, including P_4S_3, P_4S_4, P_4S_5, P_4S_7, P_4S_8, P_4S_9, and P_4S_{10}, all of which form cage-like molecular clusters.[20−27] Characterization of the various phosphorus sites found in these crystals has been accomplished with solid-state NMR.[28−31] Additionally, the phosphorus−sulfur glasses have been studied with solid-state NMR, including MAS and $^{31}P-^{31}P$ dipole second moment experiments and Raman spectroscopy.[31,32] In PS glasses, it was found that the majority of the phosphorus throughout the entire glass forming range occurs as $S{=}PS_{3/2}$ units, which are randomly distributed throughout the material. Evidence for molecular P_4S_9 and P_4S_{10} was found when phosphorus content exceeded 15 atom-%.

II. Experimental Procedures

A. Sample Preparation and Bulk Characterization. $(GeS_2)_{1-x}(P_2S_5)_x$ glasses were synthesized from 25 g mixtures of high purity elements that were loaded into 10 mm i.d. fused silica ampules under dry N_2. Prior to batching, the ampules were etched in 5%HF:5%HNO_3, rinsed in deionized water, and then dried at about 1000 °C. The filled ampules were evacuated to 10^{-6} Torr, flame sealed, and then heated to 925 °C in a rocking furnace. Following a 48 h hold at 925 °C, the furnace temperature was reduced to 850 °C for 10 min, after which cylindrical 12 cm long glass rods were formed by quenching the hot ampules in water.

Density was measured in water to ±0.001 gm/cm^3 using the Archimedes method. The glass transition temperature (T_g) was determined with a precision of ±5 °C by differential scanning calorimetry (DSC) using a heating rate of 10 °C/min. The refractive index was measured to ±0.01 by the apparent depth method at 589 nm with 5 mm thick samples.

B. NMR Measurements. The high-speed MAS experiments were performed at 161.977 MHz (9.4 T) on a Bruker Avance 400 spectrometer with a 2.5 mm Bruker MAS probe. Measurements were made at a spinning rate of 29 kHz. A 1 μs pulse length was used, corresponding to a nutation angle of 25°. This allowed recycle times to be shortened to 1−5 min, depending on the sample. T_1 for these samples ranged from 2 to 12 min. A sweep width of 100 kHz was used.

The ^{31}P 2D-PASS spectrum, for the 16.7% P_2S_5 glass, was recorded using a 7 mm Bruker MAS probe on a Bruker Avance 400 spectrometer with a 3.7 μs, $\pi/2$ pulse length, and a 120 s recycle delay. A total of 243 transients together with 4 dummy scans were accumulated at each phase shift. A spinning frequency of 6 kHz was used. The 40% P_2S_5 glass ^{31}P 2D-PASS spectrum was recorded on a Tecmag Libra spectrometer at 81.211 MHz (4.7 T), with a 4 μs, $\pi/2$ pulse length, a 120 s recycle delay, accumulation of 512 transients with 4 dummy scans, at a spinning frequency of 3 kHz. PASS π pulse timings were calculated according to Antzutkin et al.[33]

The dipole second moment experiments were performed at 81.211 MHz (4.7 T) on a Tecmag Libra spectrometer. A sweep width of 100 kHz was used. A nonspinning sample was used with a 4 μs, $\pi/2$ excitation pulse. The spin−echo intensity was collected for 10 separate dephasing times covering a range from 50 to 450 μs. Recycle delays for these experiments were 30−60 min. Calibration was done on crystalline P_4S_{10} and Ag_3PO_4.

All ^{31}P NMR spectra were referenced to 85% H_3PO_4.

C. Neutron Diffraction Measurements. The neutron diffraction experiments were performed at the pulsed neutron source ISIS, Rutherford Appleton Laboratory, Chilton, Didcot, U.K., on the time-of-flight liquid and amorphous diffractometer (LAD). LAD was equipped with detector banks positioned at seven different scattering angles from 5° to 150°. Time-of-flight spectra are recorded separately at each detector and individually corrected for background and container scattering, absorption, multiple-scattering, inelastic scattering, and normalized to the scattering of a vanadium rod. The correction procedure yielded the total structure factor $S(Q)$, for each sample, which was transformed to the real-space total correlation function $T(r)$. The total structure factor was truncated at $Q = 40$ Å^{-1} during transform. Because of the hygroscopic nature of the glass samples, they were removed from silica ampules, crushed into chunks, and sealed in cylindrical vanadium cans in a glovebox. No evidence for water contamination was detected.

D. Raman Spectroscopy Measurements. All Raman spectra were taken at the Purdue University Department of Chemistry laser facility. The micro-Raman instrument utilizes a 785 nm NIR diode laser as the source, a pair of holographic notch-filters to reject Rayleigh scattering, and a CCD detector. Samples were sealed in evacuated Pyrex ampules and spectra were taken by focusing the microscope on the surface of the sample through the ampule. A collection time of 15 s was used.

TABLE 1: Density, Molar Volume, Refractive Index, Glass Transition Temperature T_g, and the Second Moment M_2 of the Distribution of ^{31}P Magnetic Dipole Moments, in $GeS_2-P_2S_5$ Glasses as a Function of Composition

%P_2S_5	density st(g/cm^3)	molar volume (cm^3/mol)	refractive index	T_g (°C)	M_2 (10^6 rad^2 s^{-2})
10	2.641	16.18	2.227	354	2.5
16.7	2.558	16.09	2.215	300	
20	2.493	16.24	2.209	291	3.7
30	2.402	16.09	2.191	245	4.6
33.3	2.373	16.07	2.198	237	
40	2.326	15.98	2.187	216	8.8

III. Experimental Results

Table 1 lists the density, molar volume, refractive index, glass transition temperature, and phosphorus dipole distribution second moment for the glass samples. Figure 1 shows the high-speed ^{31}P MAS NMR spectra of the 10%, 16.7%, 20%, 30%, 40%, and 50% P_2S_5 glass samples in a field of 9.4 T (161.977 MHz resonant frequency) at a spinning rate of 29 kHz. Figure 2 shows the contour plot of the ^{31}P 2D-PASS spectra for the 16.7% P_2S_5 in a field of 9.4 T (161.977 MHz resonant frequency) at a spinning rate of 6 kHz; slices through the contours are shown in Figure 3. Figure 4 shows the total structure factors, $S(Q)$, measured by neutron diffraction, for the 10%, 20%, 33%, and 40% P_2S_5 glass samples; Figure 5 shows the total correlation function, $T(r)$, for each of the glass samples measured. Figure 6 shows the Raman spectra collected for the 10% through 40% P_2S_5 glass samples.

IV. Discussion

A. Density and the Glass Transition Temperature. Table 1 shows that, as the P_2S_5 content increases, there is an almost linear decrease in the mass density of $(GeS_2)_{1-x}(P_2S_5)_x$ glasses.

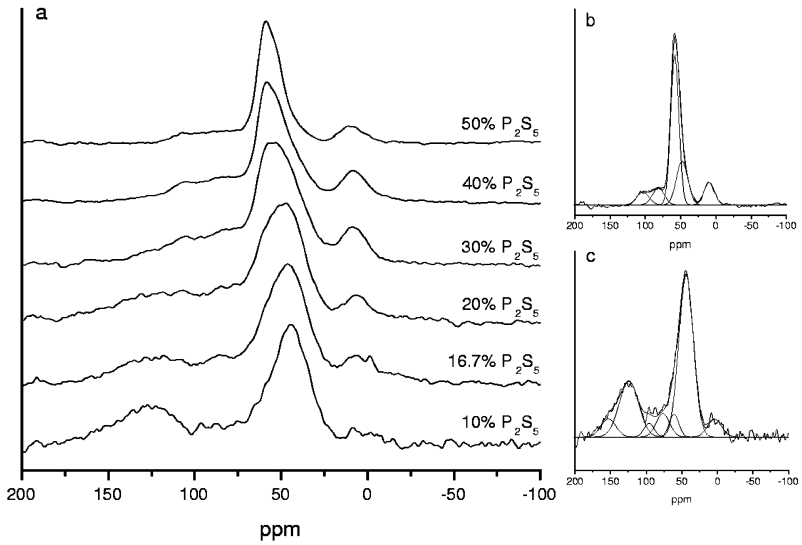

Figure 1. (a) High speed ^{31}P MAS NMR for 10%, 16.7%, 20%, 30%, 40%, and 50% P_2S_5 glass samples. Spectra were taken at 9.4 T (161.977 MHz) and a spinning rate of 29 kHz. Referenced to H_3PO_4. (b) Deconvolution of spectrum for the 40% sample; (c) same for the 10% sample. Results of deconvolutions are given in Table 2.

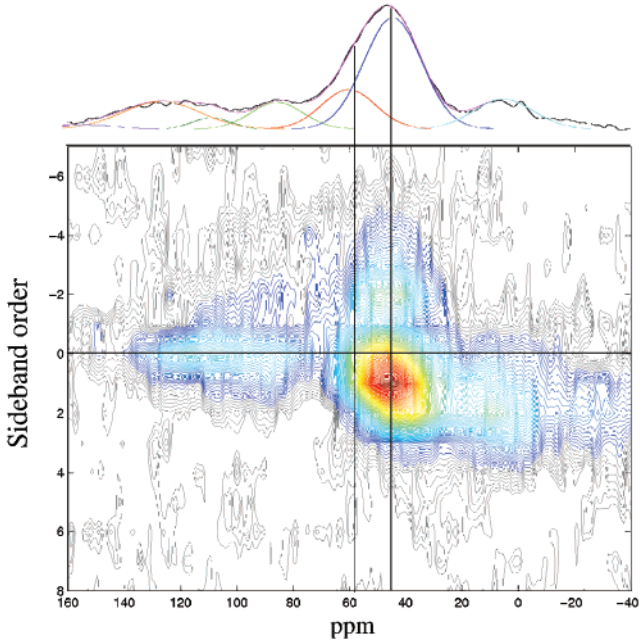

Figure 2. Contour plot of ^{31}P 2D-PASS data for the 16.7% glass sample. Spectra were taken at 9.4 T (161.977 MHz) and a spinning rate of 6 kHz. Referenced to H_3PO_4 at 0 ppm.

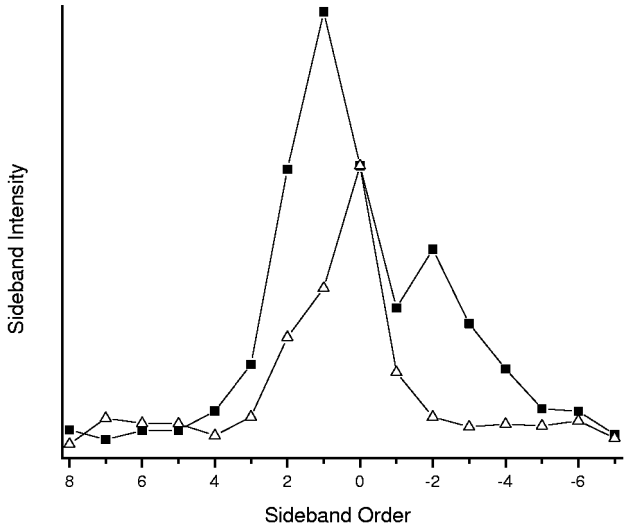

Figure 3. Slices through the 2D spectrum in Figure 2 at 44 (■) and 58 ppm (△), the isotropic shifts of the two upfield phosphorus sites, showing the sideband envelopes of these sites. Both slices are normalized to unity at the isotropic (sideband zero) shifts. The 44 ppm site shows a large negative anisotropy and small asymmetry, whereas the 58 ppm site has a smaller, positive anisotropy. See Table 4 for details.

The molar volumes given in Table 1 are atomic volumes, as they are calculated with formulas of the type $Ge_xP_yS_{1-x-y}$ rather than $(GeS_2)_{1-x}(P_2S_5)_x$. The molar volume is nearly constant, decreasing slightly with P_2S_5, indicating that the packing density does not change significantly.

The glass transition temperature decreases significantly with increasing P_2S_5 content (Table 1). Such a decrease is conventionally explained in terms of network cleavage or reduction in the number of atomic constraints; we will explore these hypotheses further after determining details of the structure.

B. Local Phosphorus Environments from NMR. The high-speed MAS spectra, Figure 1, yield the isotropic chemical shift, δ_{iso}, for the phosphorus sites present in the glasses. The spectra can be fit with six Gaussian peaks, centered roughly at 123, 103, 81, 58, 44, and 8 ppm. The intensities of these features are strongly dependent upon composition. Peak shifts, intensities, and widths are listed in Table 2. The most intense feature in the spectra appears to shift downfield from 44 to 58 ppm with increasing P_2S_5 content. In actuality, this is not simply a shift but the growth of the 58 ppm site and the loss of the 44 ppm phosphorus site, with increasing P_2S_5 content. Also, the intensity of the resonance at 123 ppm decreases to 0 as P_2S_5 content increases.

There are a variety of structural features to consider in assigning the phosphorus chemical shifts to local bonding geometries. First in importance is the local bonding neighborhood, and from the fact that no negative shifts are seen, the presence of P−Ge and P−P bonding can immediately be ruled out.[34] We thus conclude that all phosphorus are bound to sulfur, as might be expected for these stoichiometric compositions. Assigning the observed resonances to specific P−S units still requires analysis of several possible effects on the chemical shift,

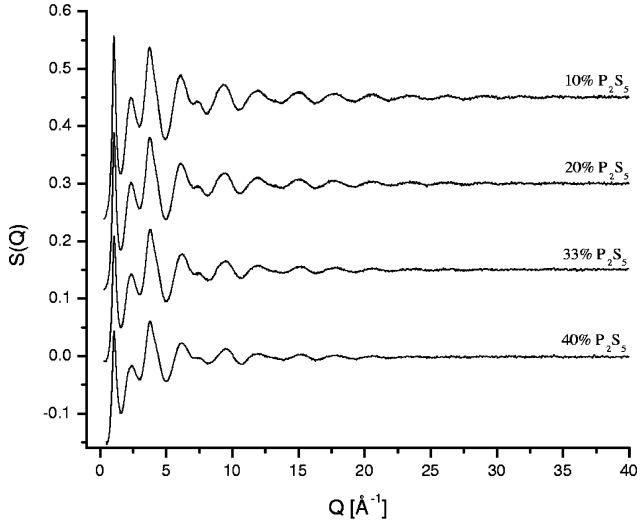

Figure 4. Total structure factors for 10%, 20%, 33%, and 40% P_2S_5 glass samples, from neutron diffraction.

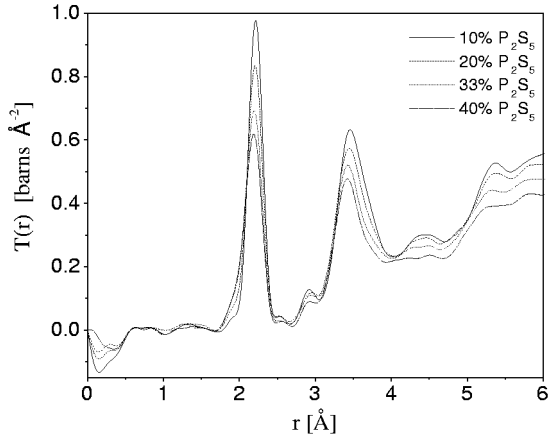

Figure 5. Total correlation functions, $T(r)$, for the 10%, 20%, 33%, and 40% P_2S_5 glass samples, from Fourier transformation of the data in Figure 4.

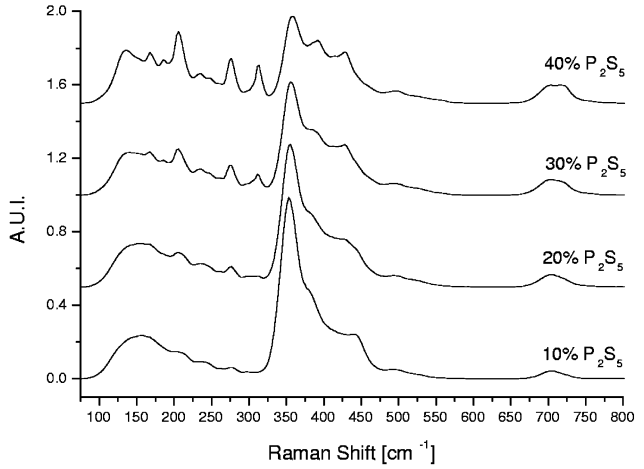

Figure 6. Raman spectra of the 10%, 20%, 30%, and 40% P_2S_5 glass samples.

including P−S coordination number, strain in the P−S polyhedron, and second neighbor effects.

Previous work on P−S crystalline and glassy systems, by H. Eckert et al.,[30,31,35] was critical in assessing these possible effects. In addition to the well-known and expected dependence of chemical shift on coordination number, Eckert suggested that strain may also play a significant role in the chemical shift of phosphorus sites in PS compounds.[35] To better define this effect, we compared the chemical shift of a series of organo-substituted S═$PS_{3/2}$ and $PS_{3/2}$ molecules with their structure.[24,26,34,36−38] The isotropic chemical shifts for the model compounds are listed in Table 3. This table also lists the bond angles that define the PS polyhedra of the molecules whose crystal structures are known. The P−S and P═S bond distances, for all of the model compounds, are the same.

From the data listed in Table 3, it appears that the geometry of the PS polyhedra is the major effect determining the isotropic chemical shift. The isotropic chemical shift, δ_{iso}, of S═$PS_{3/2}$ units can be separated into two groups, a downfield cluster of the organo-substituted molecules and isolated (from other phosphorus) network phosphorus as found in PS glass and an upfield cluster of the S═$PS_{3/2}$ sites in the cage compounds P_4S_9 and P_4S_{10}. The $PS_{3/2}$ sites can be similarly grouped. We classify the downfield group as isolated or nonstrained phosphorus sites and the upfield group as strained sites. From examination of the crystal structures of these molecules, one can see that the isotropic chemical shift is correlated with the geometry of the PS polyhedron. Units with ideal tetrahedral bond angles fall in the upfield group (e.g., P_4S_{10} with 109.6° and 109.3° S−P−S bond angles), whereas sites unconstrained by molecular cages show elongated polyhedra and fall in the downfield group (e.g., S═$P(SPh)_3$ with 117.1° and 100.9° S−P−S bond angles). This shift is evidently produced because as the polyhedron is compacted more electron density is centered about the phosphorus atom, thus increasing the shielding. Furthermore, the δ_{iso} in the model compound S═$P(SSnMe_3)_3$ suggests that second neighbor effects are secondary to changes in the PS polyhedron geometry. Its δ_{iso} is on the upfield edge of the nonstrained S═$PS_{3/2}$ cluster, and the geometry of the PS polyhedron is intermediate between that of S═$P(SPh)_3$ and the S═$PS_{3/2}$ sites

TABLE 2: Fits to 29 KHz ^{31}P MAS NMR Spectra, Including Isotropic Shifts, Relative Intensities, and Peak Widths (Shifts and Widths in ppm, Shifts Relative to 85% H_3PO_4)

$\%P_{2S5}$	intensity	fwhm	intensity	fwhm	intensity	fwhm
	123 ppm		103 ppm		81 ppm	
10	0.344	32.0	0.086	16.7	0.144	22.5
16.7	0.248	32.0	0.103	15.4	0.240	21.7
20	0.223	31.2	0.120	16.2	0.327	24.5
30	0.192	32.0	0.198	20.0	0.402	21.1
40	0.058	30.0	0.198	20.3	0.298	25.0
50			0.087	20.3	0.114	19.7
	58 ppm		44 ppm		8 ppm	
10	0.141	16.0	1.000	24.1	0.113	23.1
16.7	0.354	22.5	1.000	24.2	0.268	24.8
20	0.391	16.9	1.000	24.0	0.213	22.2
30	0.984	17.6	1.000	24.9	0.433	19.7
40	1.000	14.2	0.705	23.9	0.344	21.6
50	1.000	13.6	0.293	19.1	0.149	17.6

TABLE 3: Correlation of S═$PS_{3/2}$ and $PS_{3/2}$ Polyhedra with Geometry and Isotropic Chemical Shift[24,26,34,36−38]

	S═$P(SR)_3$			$P(SR)_3$	
R	δ_{iso} (ppm)	∠S═P−S	∠S−P−S	δ_{iso} (ppm)	∠S−P−S
Ph	91.1	117.1	100.9	130.5	97.5
Bu	92.6			116−117	
Et	92.0			115.6	
Me	98.5			124.5	
$SnMe_3$	79.5	114.5	104.5	116.6	
P_4S_{10}	51.6, 49.7	109.6 ± 1.3°	109.3 ± 0.8°		
P_4S_9	67.8, 64.0, 61.6	109.3 ± 0.2°	109.6 ± 0.8°	57.7	108.4

of the caged molecules. If second neighbor effects played the dominant role in determining the δ_{iso}, then, based on electronegativities, one would expect that the shift of a S═$PS_{3/2}$ site with Sn as its second neighbors would be at least as far upfield as a S═$PS_{3/2}$ site with P as its second neighbors (as found in P_4S_{10}), if not more so. However, the δ_{iso} of S═$P(SSnMe_3)_3$ is downfield of the S═$PS_{3/2}$ sites in the cage molecules for which all of the second neighbors are phosphorus. Therefore, the geometry of the PS polyhedra appears to be more important in determining the δ_{iso}.

Through the use of the model compounds and the trends in the chemical shift, the various sites present in the MAS spectra can thus be assigned. The 123 ppm site, which decreases with increasing P_2S_5 content, is assigned to $PS_{3/2}$ within the network. The 103 and 81 ppm sites are assigned to network-bound S═$PS_{3/2}$. We believe that second-neighbor effects together with strain account for the difference between these peaks: it is likely that the 103 ppm site is due to S═$PS_{3/2}$ units with predominantly sulfur second neighbors, as are found in PS glasses at low P content,[31] whereas the 81 ppm site is likely due to S═$PS_{3/2}$ units with predominantly Ge or possibly P second neighbors, though not in the form of molecular clusters. From the isotropic chemical shift alone, the 44 and 58 ppm sites cannot be unambiguously assigned to S═$PS_{3/2}$ and $PS_{3/2}$, but the significant upfield shifts indicate that both represent strained environments as found in molecular clusters such as P_4S_{10} and P_4S_9. To make a more detailed assignment for these sites, the chemical shift anisotropy will be used (see below).

Finally, although the exact origin of the peak near 8 ppm is not known, we speculate that it is from water contamination of the samples. The Ge−P−S glasses become increasingly hygroscopic as P_2S_5 content increases. It should be noted here that, in contrast to the neutron diffraction measurements, the NMR experiments could not be carried out in a controlled atmosphere and so some exposure to air (and hence water) was unavoidable.

Assignments for the resonances in the upfield region of the spectrum can be made by using additional information from the chemical shift anisotropy (CSA). The CSA arises because the distribution of the electron density is itself anisotropic. This information is suppressed under MAS conditions, to obtain high resolution, but can be used to extract more details about the local bonding environment. In particular, Eckert et al.[31] showed that S═$PS_{3/2}$ sites can be distinguished from $PS_{3/2}$ sites on the basis of the high-field shift tensor element. In S═$PS_{3/2}$, this element is due to shielding along the P═S direction and is consistently near −60 ppm; in $PS_{3/2}$, no principal tensor element is found at shifts much above 0 ppm. Thus, from the chemical shift anisotropy, $PS_{3/2}$ and S═$PS_{3/2}$ sites with similar δ_{iso} can be distinguished.

Many NMR experiments have been developed to correlate δ_{iso} with CSA in a 2D experiment, e.g., magic angle hopping,[39] magic angle turning,[40] and variable angle correlation spectroscopy.[41] These experiments reintroduce the CSA during a mixing period, thereby labeling each δ_{iso} with its CSA. Because of the long relaxation times in the present samples, we chose to use the 2D-PASS experiment[33] as a more practical alternative. 2D-PASS yields a purely isotropic spectrum by separating the spinning sidebands by order into a second dimension. Because the sidebands are retained, the CSA information contained in them is also retained. In contrast to the other correlation methods mentioned above, in 2D-PASS, it is only necessary to carry out the number of experiments in the first dimension corresponding to the number of sidebands observed, making the experiment practical for samples with long relaxation times. A contour plot, Figure 2, can be made for the 2D-PASS spectra by shifting the ω_1/ω_r dimension by the appropriate multiple of the rotor frequency, ω_r. Slices taken through the ω_1/ω_r dimension yield the intensities of the spinning sideband manifold for a given δ_{iso}. From this manifold, the standard Herzfeld−Berger analysis[42] can be applied to extract the chemical shift tensor elements.

TABLE 4: Chemical Shift Tensor Elements for the 44 and 58 ppm Slices Taken from the 2D-PASS Data for the 16.7 % P_2S_5 and 40 % P_2S_5 Glasses

% P_2S_5	PS unit	δ_{iso} (ppm)[a]	$\Delta\delta$ (±20 ppm)[b]	h (± 0.2)[c]	δ_{11} (ppm)[d]	δ_{22} (ppm)[d]	δ_{33} (ppm)[d]
16.7	S═$PS_{3/2}$	44	−235	0.3	154	102	−122
	$PS_{3/2}$	58	+100	0.6	5	45	125
40	S═$PS_{3/2}$	44	−250	0.3	152	102	−122
	$PS_{3/2}$	58	+120	0.5	−22	58	138
	S═$PS_{3/2}$	58	−250	0.3	166	116	−109

[a] $\delta_{iso} = 1/3(\delta_{11} + \delta_{22} + \delta_{33})$. [b] $\Delta\delta = \delta_{33} - 1/2(\delta_{11} + \delta_{22})$. [c] $\eta = \delta_{22} - \delta_{11}/\delta_{33} - \delta_{iso}$. [d] $|\delta_{33} - \delta_{iso}| \geq |\delta_{11} - \delta_{iso}| \geq |\delta_{22} - \delta_{iso}|$.

2D-PASS data were collected for the 16.7% (Figures 2 and 3) and 40% P_2S_5 glasses (spectra not shown). Table 4 contains the chemical shift tensor elements, which reproduce the sideband manifolds of slices taken at 44 and 58 ppm. For the 16.7% P_2S_5 glass, the derived tensor elements immediately show that the resonances reflect fundamentally different phosphorus sites. The 44 ppm site has its most upfield tensor element at −122 ppm, whereas the 58 ppm site's most upfield component is at 5 ppm. Because the 44 ppm site has one chemical shift component with significant shielding (much more even than the −60 ppm observed in PS crystals[31]), we assign this resonance to strained S═$PS_{3/2}$ units. We assign the 58 ppm site to strained $PS_{3/2}$ units. In the 40% P_2S_5 glass, a similar assignment can be made. Once again, the sideband manifold of the 44 ppm peak indicates the presence of a strongly shielded chemical shift tensor component and is thus assigned to a S═$PS_{3/2}$ unit. The sideband manifold for the 58 ppm slice is much narrower than that observed for the 44 ppm slice but is different from the manifold seen in the 16.7% glass. The sideband manifold for the 58 ppm slice of the 40% P_2S_5 glass appears to consist of two overlapping sideband patterns, because of both $PS_{3/2}$ and S═$PS_{3/2}$. The sideband manifold was simulated using the chemical shift tensor elements from the $PS_{3/2}$, 58 ppm, site of the 16.7% glass and an S═$PS_{3/2}$ site with the same chemical shift anisotropy and asymmetry parameter as the S═$PS_{3/2}$, 44 ppm, site of the 16.7% glass but shifted to a δ_{iso} of 58 ppm. The manifold was best fit by 60% S═$PS_{3/2}$ and 40% $PS_{3/2}$. From the fit to the 29 kHz MAS spectra, there is peak overlap from the 44 ppm site at 58 ppm, which gives rise to approximately 23% of the intensity at 58 ppm. When this overlap is factored out of the sideband manifold, it suggests that the 58 ppm peak in the 40% sample consists of 50% strained $PS_{3/2}$ and 50% strained S═$PS_{3/2}$ units.

C. Phosphorus Distribution from Spin−Echo Measurements. The second moment of the phosphorus−phosphorus magnetic dipole couplings, M_2, was measured using a spin−echo experiment with variable dephasing times.[31,43,44] M_2 contains information on the average distance between phosphorus atoms and is given by

$$M_2 = \frac{4}{15}\left(\frac{\mu_0}{4\pi}\right)^2 I(I+1)\gamma^4\hbar^2 N^{-1}\sum_{j,k} r_{jk}^{-6} \qquad (4.1)$$

where $\mu_0/4\pi$ is the permittivity of free space, I is the spin quantum number, γ is the gyromagnetic ratio, N is the number of nuclei, and r_{jk} is the distance between nuclei j and k.[44] The

intensity of the echo resulting from the spin−echo experiment decreases as the echo is refocused further out in time, because the magnetic dipole interactions are not refocused by the pulse sequence. The rate of dephasing is characterized by the second moment, M_2. At short times, the echo intensity is well described by a Gaussian

$$I(2\tau)/I(0) = \exp\lfloor -M_2(2\tau)^2/2 \rfloor \qquad (4.2)$$

where $I(2t)$ is the echo intensity for dephasing time t.[45,46] Thus, plots of $\ln[I(2\tau)/I(0)]$ versus $(2t)^2$ yield M_2 from the slopes.

Measurement of M_2 provides information on the distribution of phosphorus in the Ge−P−S system. The 10%, 20%, 30%, and 40% P_2S_5 glasses were measured; the results are given in Table 1. To understand the type of intermediate range structure present in the glasses, M_2 was calculated for a random distribution of phosphorus atoms. The model consisted of 1000 P atoms placed in a box with the same number density as the respective glass and a P−P closest approach distance of 3.4 Å (based on P_4S_{10}) to exclude P−P bonding. This model yielded an M_2 value of 0.76×10^6 rad^2 s^{-2} for the 10% P_2S_5 glass and 2.5×10^6 rad^2 s^{-2} for the 40% P_2S_5 glass. The experimental values found are significantly larger than this model predicts, consistent with the idea that the phosphorus atoms are clustering. In fact, in the 40% P_2S_5 glass, the data are consistent with a majority of the phosphorus in larger groups of at least three PS polyhedra and, hence, with our assignment of the 44 and 58 ppm sites to strained S═$PS_{3/2}$ and $PS_{3/2}$ in rings or cages.

M_2 has been previously measured for the P−S glass system and for a P_4S_{10} crystal.[31] In polycrystalline P_4S_{10}, M_2 was found to be 10×10^6 rad^2 s^{-2}, and furthermore, it was shown that intramolecular interactions contributed 80% of the total M_2 value. In the PS glass system, it is known that molecular cages are present in glasses at P content of 15% and greater. M_2 mirrors these findings: M_2 for that system shows a steady increase with P content, and above 15%, P content exceeds that predicted by a random distribution. At the stoichiometric P_2S_5 composition (28.6% P), it equals that in P_4S_{10}.[31] The M_2 data for the GePS system indicate a different type of distribution. For the 10% P_2S_5 glass, M_2 is already much too large for the phosphorus to be simply randomly distributed throughout the GeS_2 network. Instead, part of the phosphorus is in random network $PS_{3/2}$ and S═$PS_{3/2}$ sites, and the rest is in the strained rings or cages. At 40% P_2S_5, clustering is even more extensive, and the total amount of PS rings or cages has increased substantially.

D. Atomic Environments from Neutron Diffraction. The experimental structure factors $S(Q)$ for the 10% through 40% P_2S_5 glass samples are shown in Figure 4. A first sharp diffraction peak (FSDP) is seen at about 1.1 Å^{-1}, essentially the same position as in GeS_2 glass.[19] This peak decreases in intensity and widens with increasing P_2S_5 content, suggesting elements of intermediate range order found in GeS_2 are also present in the $(GeS_2)_{1-x}(P_2S_5)_x$ glasses. Germanium-centered correlations are thought to be the principal contributor to the FSDP intensity.[47,48] Oscillations in $S(Q)$ are seen out to very large Q, which is evidence for well-defined short range order in the form of Ge−S bonds.

Figure 5 shows $T(r)$ for the 10% through 40% P_2S_5 glass samples. The first intense peak, at about 2.23 Å, decreases steadily in intensity with increasing P_2S_5 content. This feature is asymmetric on the short distance side. The asymmetry arises from two peaks, at 1.89 and 2.09 Å, which increase in intensity with P_2S_5 content. The next feature seen, at about 2.9 Å, is nearly constant with P_2S_5 concentration. A large peak at about 3.5 Å decreases with P_2S_5; it has a shoulder at 3.8 Å, which only slightly decreases with P_2S_5 content. The six features described above were fit in $T(r)$ for each sample. Figure 7 shows the fit to $T(r)$ for the 40% P_2S_5 glass sample. No attempt to fit $T(r)$ above 4.0 Å was made because of the difficulty in resolving features at such large distances in amorphous materials. Each of the six peaks fit to $T(r)$ can be assigned on the basis of known atom interactions found in crystalline materials and the trends in $T(r)$ as a function of sample composition.

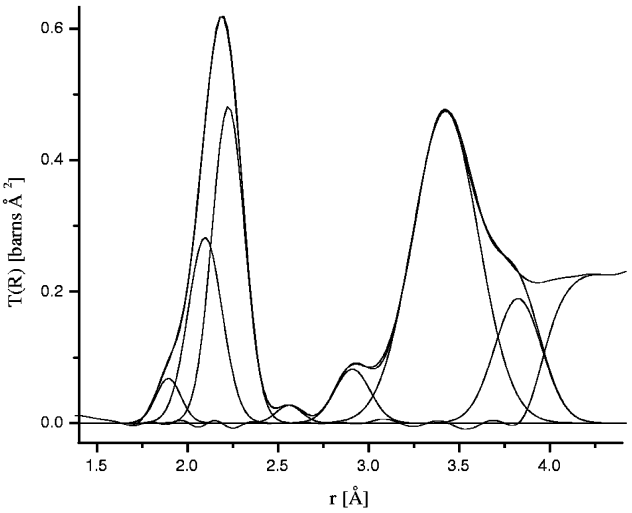

Figure 7. Representative fit to $T(r)$ with Gaussians, for the 40% P_2S_5 glass sample.

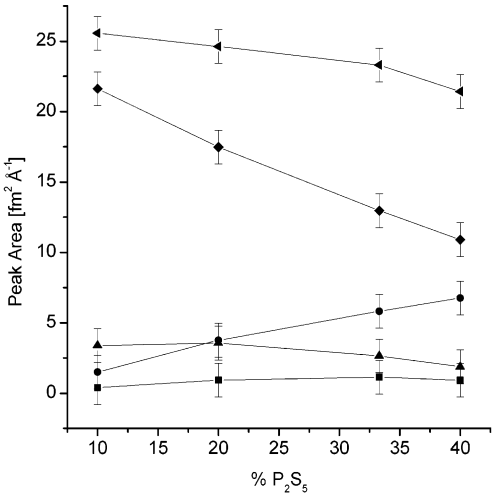

Figure 8. Trends in intensities of peaks in $T(r)$ (Figure 5, Figure 7) as function of P_2S_5 content: (■) peak one (1.89 Å); (●) peak two (2.09 Å); (◆) peak three (2.23 Å); (▲) peak four (2.92 Å); (shaded reverse arrow) peak five (3.43 Å).

As noted, the asymmetry of the first peak in $T(r)$ is due to the growth of two peaks at 1.89 and 2.09 Å. The 1.89 Å peak is assigned to phosphorus−sulfur double bonds, and the second is assigned to both P−S bonds and S−S bonds. The areas of these peaks increase as a function of P_2S_5 content, reinforcing the assignment (Figure 8). Unfortunately, the signal-to-noise ratio of $T(r)$ is not sufficient to use these peaks to make an independent determination of the relative amounts of S═$PS_{3/2}$ and $PS_{3/2}$ units in each sample, but one can conclude from the neutron diffraction data that both types of sites are present at all P_2S_5 compositions.

The third peak, at 2.23 Å, is assigned to germanium bonded to sulfur. This distance matches well with Ge−S bond distances

found in both GeS_2 crystal and glass. The area of this peak decreases systematically with increasing P_2S_5 content, corroborating this assignment. The average coordination number of sulfur about germanium calculated for this peak ranges between 3.96 and 4.04 over the compositions studied, thus every germanium is coordinated by four sulfur atoms.

The fourth peak, at 2.92 Å, is further evidence that the GeS_2 network in the $(GeS_2)_{1-x}(P_2S_5)_x$ glasses is similar to the network found in GeS_2 glass. A similar peak was seen in both neutron diffraction[19] of GeS_2 glass and an X-ray diffraction study of GeS_x glasses,[17] for $x > 2$. This distance is the Ge−Ge distance found in edge-sharing $GeS_{4/2}$ polyhedra. In our samples, the area of this peak is constant within experimental error as a function of P_2S_5.

The final two peaks in $T(r)$ which were fit, at 3.43 and 3.82 Å, are far enough out in space that many different interactions contribute to these features, so assignment becomes much more difficult. The peak at 3.43 Å has contributions from Ge−Ge and S−S pairs. Furthermore, Ge−S and P−S have approximately the same bond length, so Ge−P correlations also contribute to the area of this peak. The S−S interaction referred to is the distance between the sulfur in the same tetrahedral unit, whereas the Ge−Ge and Ge−P interactions are the distance between germanium or phosphorus of connected polyhedra. The sixth and final peak fit to $T(r)$, at 3.82 Å, might correspond to the sulfur−sulfur distance present in the Ge_3S_3 six-membered rings as found in crystalline GeS_2.

E. Raman Spectroscopy. Figure 6 shows the Raman spectra for the stoichiometric $(GeS_2)_{1-x}(P_2S_5)_x$ glasses. All of the germanium at these compositions is present in $GeS_{4/2}$ units, as shown by neutron diffraction. The $GeS_{4/2}$ polyhedra are characterized by the A_1 mode at 345 cm^{-1} and the shoulder, clearly seen in the 10% P_2S_5 sample, around 370 cm^{-1} from the F_2 companion mode.[49,50] In fact, the range from 330 to 460 cm^{-1} of the 10% P_2S_5 sample closely resembles the same region of the Raman spectrum of GeS_2 glass.[49,50] Turning to modes involving phosphorus, the bands around 700 cm^{-1} are vibrations of P═S bonds, confirming the presence of $S{=}PS_{3/2}$ units. An interesting and very informative feature of the Raman spectra, is the presence of vibrational bands at 490 cm^{-1} for all of the stoichiometric glasses. The 490 cm^{-1} band indicates that S−S bonding is present in all of the samples.[49,50] The band at 416 cm^{-1}, clearly seen in the 40% P_2S_5 sample, is from $PS_{3/2}$ units.[8,32] This complements our ^{31}P MAS NMR assignment, which also detected the presence of trigonal phosphorus in all of the glasses. Finally, the sharp bands at 210, 280, and 305 cm^{-1} suggest the presence of molecular P_4S_{10} and P_4S_9, again in agreement with our NMR results, which indicate partial clustering of phosphorus in strained environments.

F. Summary of the Structural Model. Combining the results of the NMR, neutron diffraction, and Raman experiments yields structural models for GeS_2−P_2S_5 glasses, which are summarized in Table 5 and Figure 9. Summarizing all of the data, we have found that the germanium is exclusively present as $GeS_{4/2}$ tetrahedra; the phosphorus exists in two types of sites: $PS_{3/2}$ and $S{=}PS_{3/2}$, and that these sites are found both dispersed through the network and as components of clusters, most reasonably P_4S_{10} and P_4S_9 molecular species; and finally that the sulfur connects the Ge and P polyhedra, with "excess" sulfur (produced by loss of the double-bonded capping sulfur when $PS_{3/2}$ is formed) forming −S−S− and possibly longer chains. The various features are summarized in Figure 9.

In Table 5, the amounts of the various features noted above are quantified to the extent our data sets allow. Note that $PS_{3/2}$ units, which would not be expected intuitively at these stoichiometric compositions, are a significant fraction of the phosphorus content. The NMR results suggest the presence both of strained PS units and of PS unit clustering. The Raman spectra show conclusively the presence of molecular PS species at high P_2S_5 composition, which would account for the features of the NMR spectra just noted, whereas at low P_2S_5 compositions, the strained, clustered sites may be present primarily as rings connected to the rest of the glass network. Finally, because of the significant amount of $PS_{3/2}$ units, −S−S− bonding is found at all compositions.

TABLE 5: Estimated Atomic Fractions of Phosphorus, Sulfur, and Germanium Participating in Various Bonding Units[a]

	nonstrained (network)		strained (ring/cage)				
% P_{2S5}	$PS_{3/2}$	$S{=}PS_{3/2}$	$PS_{3/2}$	$S{=}PS_{3/2}$	S−Ge, S−P	S−S	Ge−S
10	0.012	0.008	0.002	0.037	0.662	0.014	0.265
16.7	0.012	0.016	0.008	0.055	0.662	0.020	0.227
20	0.011	0.023	0.010	0.061	0.663	0.021	0.211
30	0.010	0.031	0.025	0.077	0.655	0.035	0.167
40	0.004	0.038	0.038	0.093	0.653	0.043	0.130

[a] The estimates are made based on NMR MAS and PASS ^{31}P spectral peak areas for the phosphorus units; neutron diffraction for the Ge−S unit; the $PS_{3/2}$ content for the S−S composition (all $PS_{3/2}$ units contribute an excess S atom over stoichiometry, leading to an S−S bond); and finally the S−Ge and S−P units together account for the remaining sulfur.

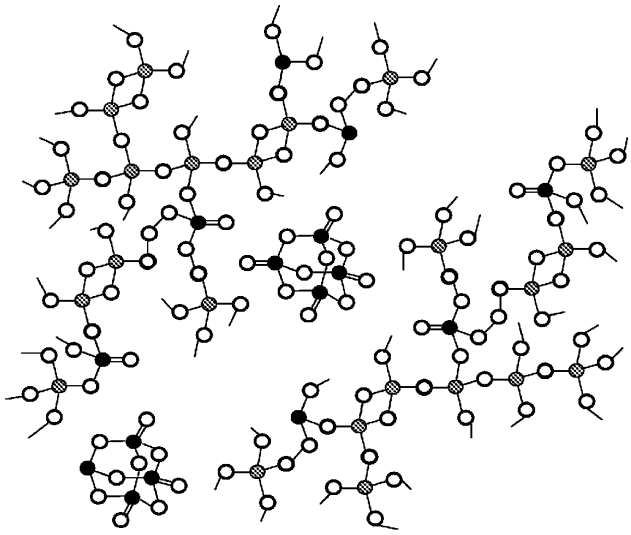

Figure 9. Pictorial representation of the structural features found in Ge−P−S glass. Ge, shaded circles; P, filled circles; S, open circles.

We turn now to correlations of the structure with bulk properties.

G. Correlation of Refractive Index with Composition. The refractive index of the $(GeS_2)_{1-x}(P_2S_5)_x$ glasses decreases with the addition of P_2S_5 (see Table 1). The refractive index here was measured at 589 nm and thus is nonresonant; it can be expressed in terms of the linear optical susceptibility χ_1 by

$$n^2 = 1 + 4\pi\chi_1 \tag{4.3}$$

The susceptility χ_1 itself can be modeled in terms of polarizabilities of the various bonds in the material, here Ge−S, S−S, and P−S.[51] The contributions to χ_1 from each bond can be expressed in terms of the bond covalency α_c and bond length d, the electron density N, and an orbital overlap matrix element

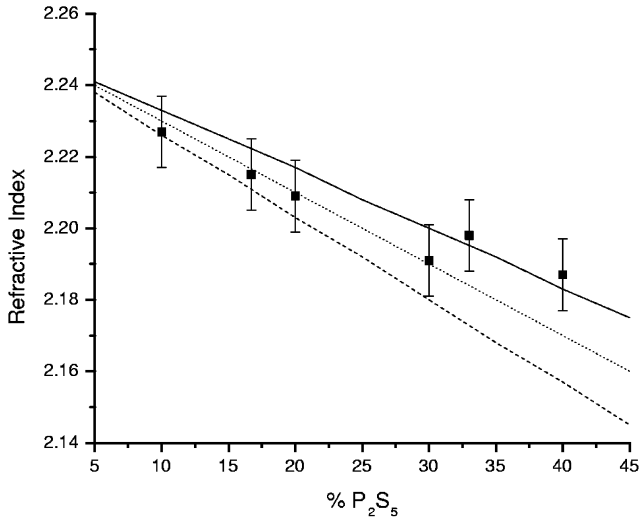

Figure 10. Comparison of refractive index with that calculated based on the bond polarizability model proposed by Harrison.[51] Solid line, all S═$PS_{3/2}$; long dashes, all $PS_{3/2}$; short dashes, equal amounts of S═$PS_{3/2}$ and $PS_{3/2}$.

V_2 for bonded atoms. The result for the contribution to χ_1 for a particular bond type is then[51]

$$\chi_1 = \frac{Ne^2\gamma^2d^2\alpha_c{}^3}{12V_2} \tag{4.4}$$

where e is the electron charge and γ is a scaling parameter. Then a compositionally weighted sum is calculated to generate the refractive index for the $(GeS_2)_{1-x}(P_2S_5)_x$ glass samples. Figure 10 shows the agreement with the calculated refractive index with the experimental values. The trend of decreasing refractive index with increasing P_2S_5 content is a result of replacing more polarizable Ge−S bonds with less polarizable P−S and S−S bonds. The magnitude and slope of the compositional dependence of n is reproduced quite well by the model. Details of the material structure are not necessary in this model, except for the correct identification of types of bonds formed (Ge−S, S−S, and P−S only, no Ge−Ge or P−P). Similarly good agreement is obtained regardless of the distribution of phosphorus between S═$PS_{3/2}$ and $PS_{3/2}$ sites, because of the similar polarizability of the P−S and S−S bonds.

H. Correlation of Glass Transition Temperature, T_g, with Structure. Figure 11 shows the variation of T_g, the glass transition temperature, with P_2S_5 content. T_g decreases as P_2S_5 is added, which is not surprising considering that such an addition involves the replacement of four-coordinate Ge atoms by P and S atoms making, respectively, three and two connections to the network. Such variations of T_g with connectivity are seen in virtually all chalcogenide glasses. Notable here, however, is the rate of change of T_g with composition. To quantify this rate, we express the network constraints in terms of the bond density $\langle r\rangle$, the average number of bonds per atom. This quantity is calculated as $\langle r\rangle = \Sigma_i n_i r_i$, where n_i is the fraction of atomic species i in the glass and r_i is its coordination number. In the present system, allowance must be made for S═$PS_{3/2}$ units, because one-coordinate atoms contribute fewer constraints to this counting scheme.[52,53] The result, $\langle r\rangle = 4n_{Ge} + 3n_P + 2n_S$, turns out to be independent of the relative amounts of S═$PS_{3/2}$ and $PS_{3/2}$. The inset in Figure 11 shows a plot of T_g versus $\langle r\rangle$.

The inset to Figure 11 shows that as bond density and hence network constraints are removed the glass transition temperature

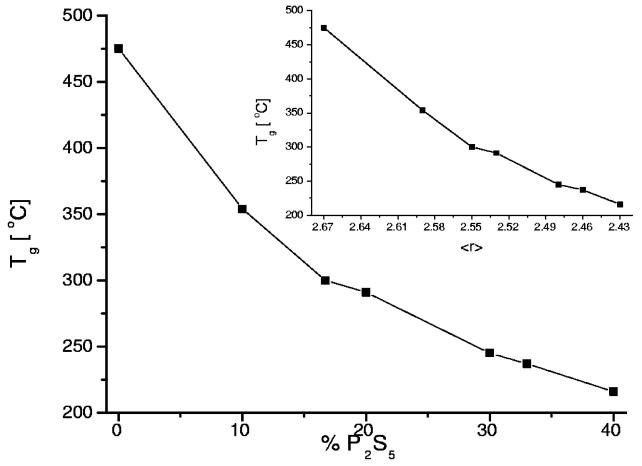

Figure 11. Glass transition temperature, T_g, as a function of P_2S_5 content. Inset: T_g as a function of bond density $\langle r\rangle$.

decreases, as expected. The rate of decrease is remarkable, when compared to many other chalcogenide systems. We estimate from our data that $dT_g/d\langle r\rangle$ is about 1300 K in the present system, whereas in Ge−As−Se, it is about 350 K,[5] and in Ge−P−Se, about 450 K.[54] This sharp temperature dependence may be due to the presence of molecular PS clusters, which would act to decrease the number of constraints much more rapidly than when the same P and S atoms participate in the network. However, in the Ge−As−S system, there is also strong evidence for molecular species,[55] but $dT_g/d\langle r\rangle$ is similar to that found in Ge−P−Se and Ge−As−Se.

The constraint argument presupposes that all atoms participate in the network, which is clearly not the case here. However, if the volume of molecular clusters is not large, they will not percolate to dominate the system, and the remaining network will be essentially intact. Table 5 shows that the relative amount of phosphorus in the network and in molecular species remains about constant at 0.5, suggesting that as the global composition changes the network reflects the total and does not show a relative excess or deficit of phosphorus. Thus, although the normal trend of a decrease in T_g with $\langle r\rangle$ is due to the network connectivity, its anomalous composition dependence is probably not a simple consequence of the presence of molecular species.

The equilibrium phase diagram for $(GeS_2)_{1-x}(P_2S_5)_x$ shows that the liquidus temperature decreases very rapidly as P_2S_5 is added, at a rate comparable to that of T_g (Figure 11), until the composition reaches a eutectic at about 30% P_2S_5.[9] At higher P_2S_5 concentrations, the liquidus is nearly independent of temperature. Quite likely, then, the composition dependence of T_g is more a reflection of the composition dependence of the liquidus temperature, rather than a special feature of the presence of molecular species. It is moreover interesting to note that the disappearance of $PS_{3/2}$ units in the network roughly coincides with the eutectic composition (Table 5) and the onset of a composition-independent liquidus temperature.[9] This coincidence may reflect the equilibrium between S═$PS_{3/2}$ and $PS_{3/2}$, which favors the former at low temperatures and the latter at high.[56] Because chemical transformations are quenched at T_g, the structure reflects the liquid composition (at least to some extent) in the glass; the high T_g at low P_2S_5 content would thus favor $PS_{3/2}$, and the low T_g at high P_2S_5 favors S═$PS_{3/2}$.

V. Conclusions

This work on the Ge−P−S glass system has resulted in a qualitative picture of the structure of this glass, generated from

the details of the short and medium range order (SRO and MRO) present (Table 5 and Figure 9). First, the neutron diffraction and Raman results show that all of the germanium are present in $GeS_{4/2}$ units. The FSDP from neutron diffraction also suggests that the GeS_2 network, as found in vitreous GeS_2, is relatively intact. As P_2S_5 is added to the system, it is incorporated into the GeS_2 network but not in a random, homogeneous fashion. The phosphorus−phosphorus dipole second moment, M_2, measurements show that the phosphorus is much more clustered than a random distribution would predict. Assignment of the types of phosphorus sites present were made from the correlation of the geometry the PS polyhedra and their δ_{iso}, together with the remarkably upfield tensor component found in $S{=}PS_{3/2}$ units because of the P═S bond. Phosphorus is found to be in both $S{=}PS_{3/2}$ and $PS_{3/2}$ sites, in contrast to PS glasses. The NMR signals at upfield shifts indicate that a significant fraction of the phosphorus in each sample is in strained environments, such as are found in the molecular clusters P_4S_{10} and P_4S_9. The Raman spectra demonstrate the presence of such molecular species.

The molar volumes of the glasses studied here are essentially constant with respect to composition, indicating that no major changes in atomic packing occur across the composition range studied. The refractive index shows a nearly linear drop as P_2S_5 is added, which was explained qualitatively based a model of susceptibility that focuses on bond polarizabilities; as the Ge−S bonds are replaced by P−S and S−S bonds, the refractive index decreases. Finally, the glass transition temperature was found to vary much more strongly with composition and bond density than in other superficially similar glass families; we conclude that, although molecular cluster formation may play some role in this variation, it is probably mainly a reflection of the liquid-state thermodynamics, which show a similarly sharp compositional dependence in the liquidus temperature.

Acknowledgment. We thank Alex Hannon (ISIS) for his assistance with the neutron experiments and Randy Youngman (Corning) for many helpful discussions. We acknowledge Mark Powley and David Crooker for their technical assistance in the synthesis of the glass samples used in this study. We thank Corning Incorporated and the NSF for financial support (DMR-9870246).

References and Notes

(1) Turnbull, D. A.; Aitken, B. G.; Bishop, S. G. *J. Non-Cryst. Solids* **1999**, *244*, 260.
(2) Aitken, B. G.; Quimby, R. S. *J. Non-Cryst. Solids* **1997**, *213*, 281.
(3) Thorpe, M. F. *J. Non-Cryst. Solids* **1983**, *57*, 355.
(4) Phillips, J. C. *J. Non-Cryst. Solids* **1979**, *34*, 153.
(5) Tatsumisago, M.; Halfpap, B. L.; Green, J. L.; Lindsay, S. M.; Angell, C. A. *Phys. Rev. Lett.* **1990**, *64*, 1549.
(6) Harris, R.; Mann, B. *NMR and Periodic Table*; Academic Press: London, 1978.
(7) Price, D. L.; Sköld, K. Introduction to Neutron Scattering. In *Neutron Scattering*; Price, D. L., Sköld, K., Eds.; Academic Press: Orlando, FL, 1986; Vol. 23A, pp 1.
(8) Koudelka, L.; Pisárčik, M. *Phys. Chem. Glasses* **1990**, *31*, 217.
(9) Vinogradova, G.; Maisashvili, N. *Russ. J. Inorg. Chem.* **1979**, *24*, 590.
(10) Aitken, B. G.; Youngman, R. E. *J. Non-Cryst. Solids* **2000**, *263&264*, 117.
(11) Aitken, B. G.; Youngman, R. E.; Ponader, C. W. *J. Non-Cryst. Solids* **2001**, *284*, 34.
(12) MacLachlan, M. J.; Petrov, S.; Bedard, R. L.; Manners, I.; Ozin, G. A. *Angew. Chem. Int. Ed.* **1998**, *37*, 2076.
(13) Prewitt, C.; Young, H. *Science* **1965**, *149*, 535.
(14) Dittmar, V.; Schäfer, H. *Acta Cryst.* **1975**, *B31*, 2060.
(15) Dittmar, V.; Schäfer, H. *Acta Cryst.* **1976**, *B32*, 1188.
(16) Armand, P.; Ibanez, A.; Dexpert, H.; Philippot, E. *J. Non-Cryst. Solids* **1992**, *139*, 137.
(17) Červinka, L.; Hrubý, A. In *Proceedings of the 5th International Conference on Amorphous and Liquid Semiconductors*; Stuke, J., Brenig, W., Eds. Garmisch-Partenkirchen, 1974; Vol. 1, pp 431.
(18) Červinka, L.; Bergerová, J. *J. Non-Cryst. Solids* **1992**, *150*, 132.
(19) Lin, C.; Busse, L.; Nagel, S.; Faber, J. *Phys. Rev. B* **1984**, *29*, 5060.
(20) Leung, Y.; Waser, J. *Acta Cryst.* **1957**, *10*, 574.
(21) Chattopadhyay, T.; Gmelin, E.; Schnering, H. V. *J. Phys. Chem. Solids* **1982**, *43*, 925.
(22) Minshall, P.; Sheldrick, G. *Acta Cryst. B* **1978**, *34*, 1326.
(23) Griffin, A.; Minshall, P.; Sheldrick, G. *J. Chem. Soc. Chem. Commun.* **1976**, 809.
(24) Vos, A.; Othof, R.; Balhuis, F. v.; Botterweg, R. *Acta Cryst.* **1969**, *19*, 684.
(25) Dixon, D.; Einstein, F.; Penfold, P. *Acta Cryst.* **1969**, *18*, 221.
(26) Hilmer, W. *Acta Cryst. B* **1969**, *25*, 1229.
(27) Demarcq, M. *Phosphorus Sulfur* **1987**, *33*, 127.
(28) Bjorholm, T.; Jakobsen, H. J. *J. Am. Chem. Soc.* **1991**, *113*, 27.
(29) Eckert, H. *Angew. Chem. Int. Ed. Engl.* **1989**, *28*, 1723.
(30) Eckert, H.; Liang, C. S.; Stucky, G. D. *J. Phys. Chem.* **1989**, *93*, 452.
(31) Tullius, M.; Lathrop, D.; Eckert, H. *J. Phys. Chem.* **1990**, *94*, 2145.
(32) Koudelka, L.; Pisárčik, M.; Gutenev, M. S.; Blinov, L. N. *J. Mater. Sci. Lett.* **1989**, *8*, 933.
(33) Antzutkin, O. N.; Shekar, S. C.; Levitt, M. H. *J. Magn. Reson. Series A* **1995**, *115*, 7.
(34) Tebby, J. *CRC Handbook of Phosphorus-31 Nuclear Magnetic Resonance Data*; CRC Press Inc.: Ann Arbor, MI, 1991.
(35) Shibao, R.; Xia, Y.; Srdanov, V.; Eckert, H. *Chem. Mater.* **1995**, *7*, 1631.
(36) Shihada, A.; Weller, F. *J. Organomet. Chem.* **1988**, *342*, 177.
(37) Shibao, R.; Keder, L.; Eckert, H. *Acta Cryst.* **1992**, *C48*, 1525.
(38) Burford, N.; Ryan, B.; White, P. *Acta Cryst.* **1990**, *C46*, 274.
(39) Bax, A.; Szeverenyi, N. M.; Maciel, G. E. *J. Magn. Reson.* **1983**, *52*, 1983.
(40) Gan, Z. *J. Am. Chem. Soc.* **1992**, *114*, 8307.
(41) Frydman, L.; Chingas, G. C.; Lee, Y. K.; Grandinetti, P. J.; Eastman, M. A.; Barrall, G. A.; Pines, A. *J. Chem. Phys.* **1992**, *97*, 4800.
(42) Herzfeld, J.; Berger, A. E. *J. Chem. Phys.* **1980**, *73*, 6021.
(43) Hahn, E. *Phys. Rev.* **1950**, *80*, 580.
(44) Van Vleck, J. H. *Phys. Rev.* **1948**, *74*, 1168.
(45) Engelsberg, M.; Norberg, R. *Phys. Rev. B* **1972**, *5*, 3395.
(46) Fenzke, D.; Freude, D.; Mueller, D.; Schmiedel, H. *Phys. Stat. Sol.* **1972**, *50b*, 209.
(47) Elliott, S. R. *Physics of Amorphous Materials*, 2nd ed.; Wiley: New York, 1990.
(48) Elliott, S. R. *Phys. Rev. Lett.* **1991**, *67*, 711.
(49) Lucovsky, G.; Galeener, F.; Keezer, R.; Geils, R.; Six, H. *Phys. Rev. B* **1974**, *10*, 5134.
(50) Lucovsky, G.; de Neufville, J.; Galeener, F. *Phys. Rev. B* **1974**, *9*, 1591.
(51) Harrison, W. A. *Electronic Structure and the Properties of Solids*; Dover: Mineola, NY, 1989.
(52) Dohler, G.; Dandaloff, R.; Bilz, H. *J. Non-Cryst. Solids* **1980**, *42*, 87.
(53) Thorpe, M. *J. Non-Cryst. Solids* **1995**, *182*, 135.
(54) Lyda, C.; Tepe, T.; Tullius, M.; Lathrop, D.; Eckert, H. *J. Non-Cryst. Solids* **1994**, *121*, 271.
(55) Aitken, B. G.; Ponader, C. W. *J. Non-Cryst. Solids* **2000**, *274*, 124.
(56) Gardner, M. *J. Chem. Soc., Dalton Trans.* **1973**, *6*, 691.